

A Two-Terminal Optoelectronic Synapses Array Based on the ZnO/Al₂O₃/CdS Heterojunction with Strain-Modulated Synaptic Weight

Xun Han, Yufei Zhang, Zhihao Huo, Xiandi Wang, Guofeng Hu, Zhangsheng Xu, Hui Lu, Qiuchun Lu, Xidi Sun, Li Qiu, Peiguang Yan,* and Caofeng Pan*

Artificial optoelectronic synapses with flexibly regulated synaptic weight are crucial to the rapidly evolved artificial visual system. Although three-terminal devices with transistor geometry have exhibited controllable synaptic response through applying electrical pulses on the gate terminal, the complicated device structure limits its integration with array configurations. In this work, a simple two-terminal optoelectronic synapses array based on the ZnO/Al₂O₃/CdS heterojunction with tunable synaptic weight is presented. It can respond to UV and green light stimulation in a neuromorphic manner, allowing the implementation of the basic synaptic function. By introducing the piezo-phototronic effect, the synaptic weight can be regulated in multilevels, extending the forgetting time by 30.08% and reducing training epochs for image recognition by 36.13%. In addition, the device can extract the target image from massive noisy optical inputs avoiding redundant data memorization. This work provides a novel method to regulate the synaptic weight of the simple two-terminal device configuration through the piezo-phototronic effect, showing potential applications for the mimicry of the human visual-perception system.

problems, which have experienced a rapid evolution over the past few years.^[1] However, the physically separated processor and memory unit limit the computational efficiency of the von Neumann machines.^[2] To imitate the advanced feature of parallel computing of the human brain, neuromorphic computing has been proposed a few decades ago and evolved recently due to the emerging of artificial synapses which emulate the synaptic functions in a neural network for information transmission and processing.^[3] The artificial synapses could be stimulated by electrical or photonic stimuli with a two-terminal or three-terminal device configuration.^[4] Optoelectronic synapses (OSs), integrating the optical information capturing, preprocessing, and memorization functions to mimic the visual-perception system, have been demonstrated to be an essential unit of the artificial neural networks (ANN)

with unique advantages of broad bandwidth, fast signal transmission, and low interconnect energy consumption.^[4c]

In biological neural networks, the connection strength between adjacent neurons, termed synaptic weight, could be

1. Introduction

Computer systems based on the von Neumann architecture possess excellent capability for solving structured mathematical

X. Han, L. Qiu
College of Mechatronics and Control Engineering
Shenzhen University
Shenzhen 518060, P. R. China

X. Han, Y. Zhang, Z. Huo, G. Hu, Z. Xu, H. Lu, Q. Lu, X. Sun, C. Pan
CAS Center for Excellence in Nanoscience
Beijing Key Laboratory of Micro-nano Energy and Sensor
Beijing Institute of Nanoenergy and Nanosystems
Chinese Academy of Sciences
Beijing 101400, P. R. China
E-mail: cfpan@binn.cas.cn

Y. Zhang, Z. Huo, Z. Xu, H. Lu, C. Pan
School of Nanoscience and Technology
University of Chinese Academy of Sciences
Beijing 100049, P. R. China

X. Wang
Department of Biomedical Engineering
Key Laboratory for Biomedical Engineering of Ministry of Education
Zhejiang Provincial Key Laboratory of Cardio-Cerebral Vascular Detection
Technology and Medicinal Effectiveness Appraisal
Zhejiang University
Hangzhou 310027, P. R. China

G. Hu, P. Yan
College of Physics and Optoelectronic Engineering
Shenzhen University
Shenzhen 518060, P. R. China
E-mail: yanpg@szu.edu.cn

 The ORCID identification number(s) for the author(s) of this article can be found under <https://doi.org/10.1002/aelm.202201068>.

© 2023 The Authors. Advanced Electronic Materials published by Wiley-VCH GmbH. This is an open access article under the terms of the Creative Commons Attribution License, which permits use, distribution and reproduction in any medium, provided the original work is properly cited.

DOI: 10.1002/aelm.202201068

regulated by controlling the physiological level of neurotransmitters to achieve various information processing efficiencies.^[5] To emulate the neuromodulation process, the three-terminal devices with transistor geometry are developed, where the gate electrodes are served as an additional terminal for applying electrical potentiation or depression.^[6] However, this additional terminal requires a specific interconnect layout and yields large unit dimensions, limiting the compatibility with large-area array configuration.^[7] A straightforward method is to construct simple two-terminal neuromorphic devices with synaptic weight modulation. Piezo-phototronic devices and integrated systems have been proposed with simplified device structures.^[8] The inner-crystal piezopotential was functionalized as the gate voltage to modulate the charge carrier generation, transport, separation, and recombination process at the junction area.^[9] Various two-terminal devices based on the non-centrosymmetric semiconductors, including ZnO, GaN, ZnS, and CdS, have been reported with an enhanced or regulated performance by the piezo-phototronic effect.^[9d,10] Thus, utilizing the abundant mechanical stimuli to introduce the piezo-phototronic effect offers a new approach to realizing multilevel synaptic response as well as to simplifying the synapse structures.

Here, we demonstrate a two-terminal ZnO/Al₂O₃/CdS heterojunction-based optoelectronic synapses (ZAC-OSs) array with the modulation of synaptic weight. Due to the strong absorption

of the UV and green light and the persistent photoconductivity (PPC) phenomenon of ZnO nanowires (NWs) and CdS film, the ZAC-OS device can respond to light stimuli in a neuromorphic manner. The synaptic weight of the device can be flexibly manipulated by external strain through the piezo-phototronic effect, showing a controllable change of the excitatory postsynaptic current (EPSC) in multilevel, reinforced memorization of the EPSC and enhancement of the image recognition rate and efficiency. Moreover, under the strain modulation, the ZAC-OSs array could derive the target image from massive noisy optical inputs, avoiding storing the redundant data for postprocessing.

2. Results and Discussion

Almost 80% of the information captured from the ambient environment is perceived by the human visual-perception system.^[11] Figure 1a schematically shows a human visual-perception system. The image information is received and converted to electrical signals by the retina, and then transmitted to the visual cortex through the neural network. A synapse, containing a presynaptic and a postsynaptic terminal, builds a connection channel between two neurons. The connection strength of a synapse, called synaptic weight, can be changed by the input stimuli, which underpins the cognitive function

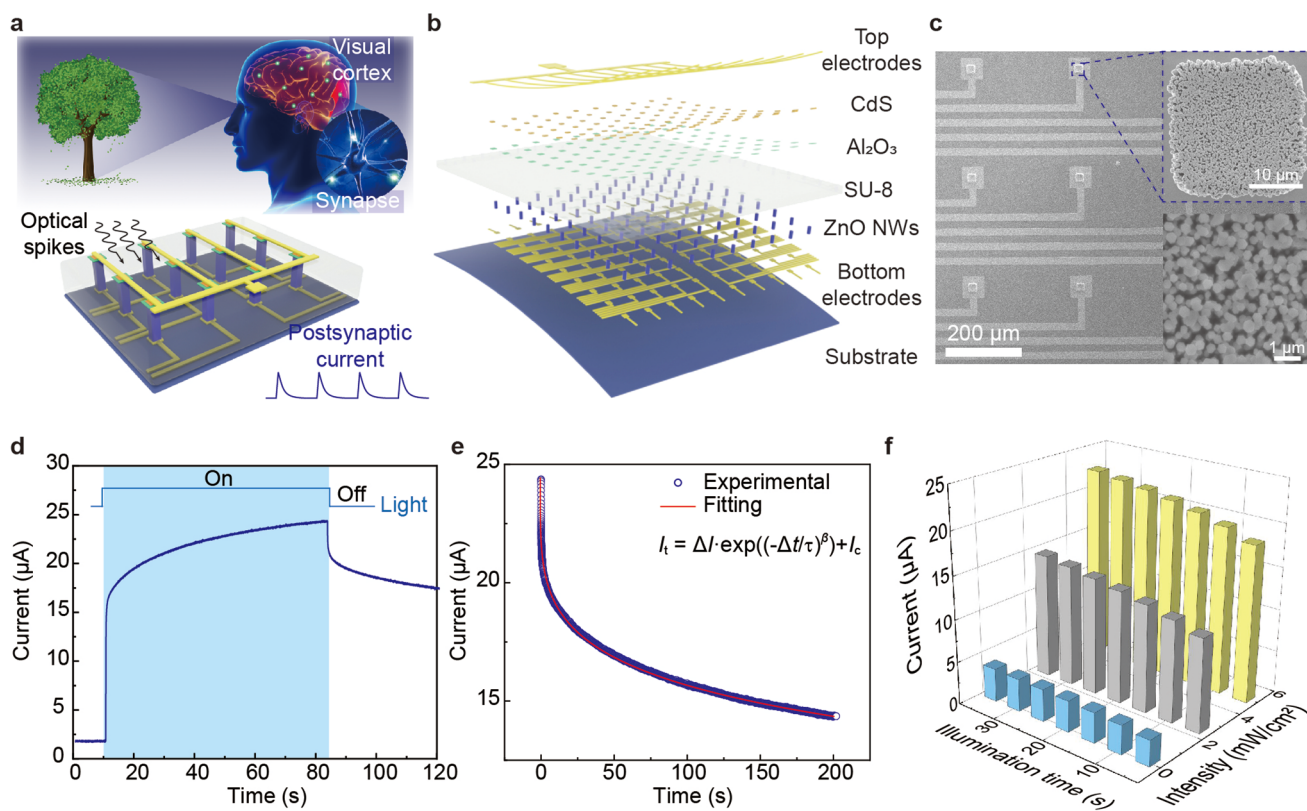


Figure 1. Device configuration and photoresponse of the ZnO/Al₂O₃/CdS-based ZAC-OSs device. a) Schematic illustration of the ZAC-OSs device to emulate the function of the human visual-perception system. b) Schematic illustration of the device structure of the ZAC-OSs device. c) SEM image of the ZnO NWs array aligned with bottom ITO electrodes. Inset: SEM image of a ZnO NWs branch (upper) and its enlarged view (lower). d) EPSC of the ZAC-OSs device under UV light illumination with a light intensity of 5.0 mW cm⁻². e) Fitting results of the decaying process of the EPSC through the Ebbinghaus forgetting curve. f) EPSC evolution process of the ZAC-OSs device under UV light illumination with various intensities.

of learning, memory, and forgetting of the brain.^[12] The key principle to mimic the human visual-perception system is to realize the photo-triggered synaptic plasticity in the ZAC-OSs device. We employed the PPC phenomenon of the ZnO/Al₂O₃/CdS heterojunction. The structure of the ZAC-OSs device is demonstrated in Figure 1b. Each pixel is regarded as a two-terminal OS, which consists of a branch of ZnO NWs, a layer of CdS film, and a thin Al₂O₃ film sandwiched between them to form a heterojunction. The UV (365 nm) and green (525 nm) light pulses are adopted as the external stimuli and the photoresponse of the device is analogous to the synaptic behavior of a biosynapse. Thus, the photocurrent is termed the EPSC. Figure S1 (Supporting Information) demonstrates the fabrication process of the ZAC-OSs array. Briefly, a layer of indium tin oxide (ITO) film was first deposited on the pre-cleaned glass substrate and patterned as the bottom electrode. Subsequently, a ZnO seed layer array was precisely formed in the center ITO electrode pad with a pixel dimension of 20 μm × 20 μm and a pitch of 300 μm. Then, the ZnO NWs were synthesized through the low-temperature hydrothermal method, followed by the SU-8 photoresist spin-coating to improve the device stability. Next, a thin layer of Al₂O₃ film (8 nm) was formed on the top of ZnO NWs through the atomic layer deposition (ALD) to passivate the trap states at the surface. Then, a layer of CdS film array was deposited to yield the ZnO/Al₂O₃/CdS heterojunction, followed by the deposition of the common top ITO electrode to complete the fabrication process. It is worth noting that the bottom electrode is connected with each branch of ZnO NWs and the top electrode contacts with all CdS pixels, which minimizes the electrode numbers of the array device and ensures that each pixel is addressable. The detailed fabrication process can be found in the Experimental Section. Figure S2 (Supporting Information) demonstrates the absorption spectra of different layers of the device, showing the strong absorption at the wavelength of 365 and 525 nm of the ZnO/Al₂O₃/CdS heterojunction. The morphology of the ZnO NWs was characterized by scanning electron microscopy (SEM), as shown in Figure 1c. The NWs are well vertically aligned and closely packed on the electrodes pad. The crystalline structures of the ZnO NWs and CdS film were analyzed by X-ray diffraction (XRD) spectroscopy (Figure S3, Supporting Information). A strong diffraction peak at 34.42° of the ZnO NWs is observed, which is ascribed to the (002) plane and indicates the wurtzite crystalline structure. The crystal phase of CdS film can be indexed to the greenockite CdS.

The structure of the ZAC-OSs device was further characterized through transmission electron microscopy (TEM). Figure S4a (Supporting Information) shows the TEM image of the ZnO/Al₂O₃/CdS heterojunction, in which one end of the ZnO NWs was covered by a thin layer of Al₂O₃ and CdS film. The typical high-resolution TEM image (HRTEM), recorded from the selected area marked in Figure S4a (Supporting Information), demonstrates the ZnO crystal lattice fringes with a plane spacing of 0.26 nm, corresponding to the (0002) plane lattice distance of hexagonal-structured ZnO, which proves that the ZnO NWs grew along *c*-axis (Figure S4b, Supporting Information). The selected area electron diffraction (SAED) pattern in Figure S4c (Supporting Information) confirms the single-crystal structure of the ZnO NWs. The element mapping

images of the ZnO/Al₂O₃/CdS heterojunction were obtained through energy-dispersive X-ray spectroscopy (EDS), as shown in Figure S4d–h (Supporting Information), identifying the formation of the heterojunction.

The photoresponse of the ZnO/Al₂O₃/CdS heterojunction presents the basic characteristics of the synaptic plasticity of the optoelectronic neural networks. Figure 1d demonstrates the change of photocurrent under continuous UV light illumination with a light intensity of 5.0 mW cm⁻². The photocurrent increases rapidly upon light illumination and tends to saturation with increased light duration. An obvious photocurrent change of ~20.68 μA is achieved with continuous illumination for 75 s. After removing the light, the gradual decay of photocurrent occurs, which is attributed to the PPC effect of the ZnO NWs array and CdS film.^[13] The decay process of the photocurrent is well fitted with Kohlrausch stretched-exponential function (Figure 1e)^[14]

$$I_t = \Delta I \cdot \exp\left[-\left(\frac{t}{\tau}\right)^\beta\right] + I_c \quad (1)$$

where τ and β are the relaxation time and the stretching exponent, respectively. I_c denotes the background current of the 1.82 μA. The τ is fitted to be 1536 s, which suggests the good nonvolatility of the photoresponse of this synaptic device. To further characterize its photoresponse behavior, the device was then exposed to UV light stimulation with various durations and intensities. As shown in Figure 1f, either a long illumination duration or high illumination intensity could give rise to large photocurrent change. Furthermore, the device could also respond to the green light (525 nm) stimulation (Figure S5, Supporting Information) and similar photoresponse behaviors, including photocurrent saturation and gradually decaying, are observed. However, the device demonstrates a more sensitive photoresponse to the UV light stimuli due to the large absorption of the UV light by both CdS and ZnO components and high external quantum yield.^[15]

Paired-pulse facilitation (PPF) is an essential short-term plasticity behavior of the neuronal networks, which is important for temporary information recognition and decoding.^[16] The PPF describes the fact that the second spike could evoke a reinforced EPSC, where the enhancement ratio depends on the time interval of these two consecutive spikes. Pulsed light stimulation is applied to the device to implement the basic synaptic function of a biosynapse. **Figure 2a** shows the EPSC under two consecutive light pulses with a time interval of 0.1 s. We utilized A_1 and A_2 to represent the EPSC change evoked by the two spikes and calculated the PPF index through A_2/A_1 . As shown in Figure 2b, the PPF index exhibits a monotonously decreasing with the time interval (Δt). Assuming it possesses a slow decay and a rapid decay process, the dependence of the PPF index on the Δt can be well fitted with the following double-exponential equation^[17]

$$\text{PPF} = c_1 \cdot \exp\left(-\frac{\Delta t}{\tau_1}\right) + c_2 \cdot \exp\left(-\frac{\Delta t}{\tau_2}\right) \quad (2)$$

where the two exponential terms describe the rapid and slow decay process, τ_1 and τ_2 represent the characteristic relaxation time of the rapid and slow decay process, and c_1 and c_2

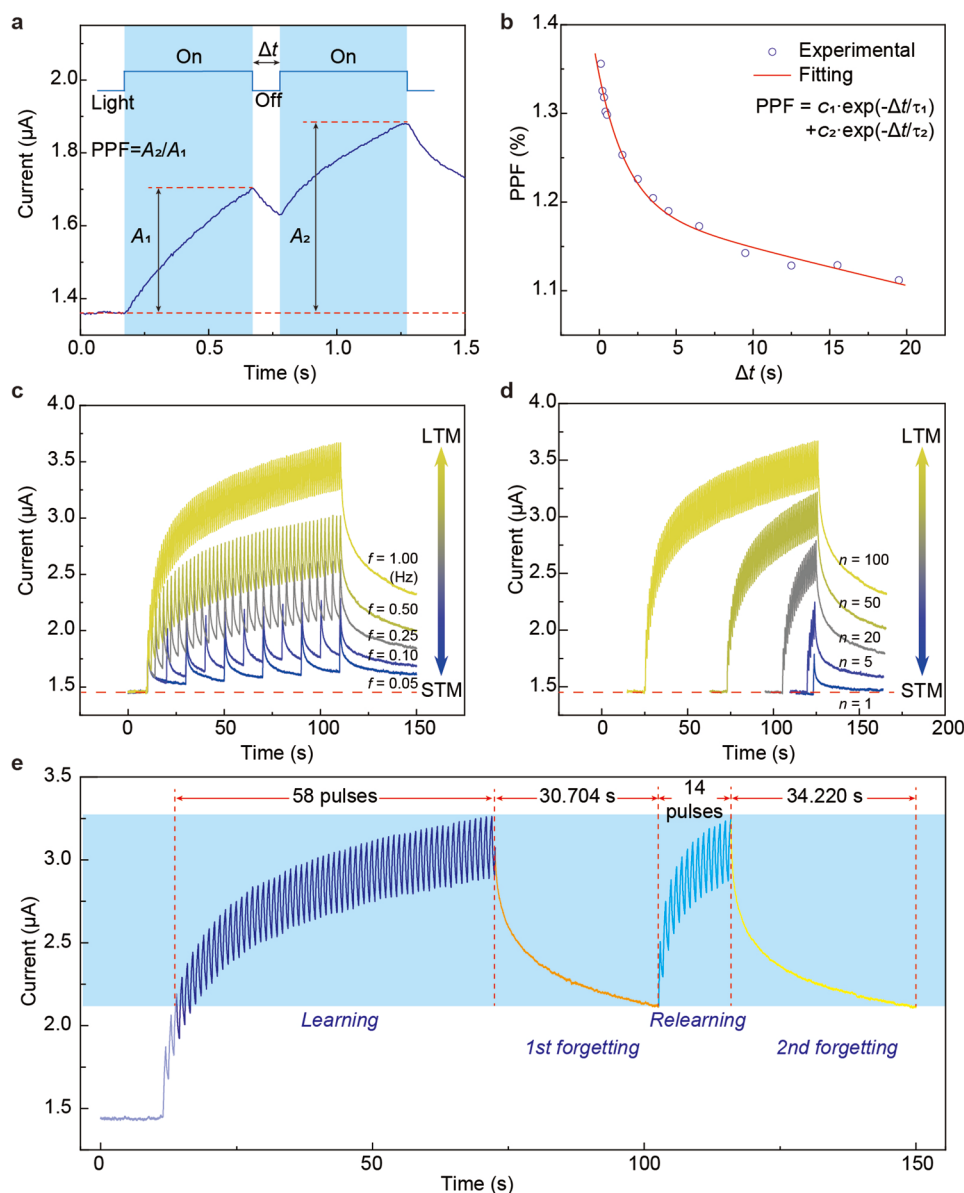


Figure 2. Basic synaptic behavior of the ZAC-OSs device under UV light stimuli. a) EPSC of the ZAC-OSs device induced by a paired light pulse with a time interval of 0.1 s. b) PPF index as a function of the time interval of the paired light pulse. c,d) The transition from STM to LTM induced by increased frequency and number of light stimuli with an intensity of 2.48 mW cm^{-2} . e) Mimic of “learning-experience” behavior under UV light stimuli with a frequency of 1 Hz and intensity of 2.48 mW cm^{-2} .

represent the initial facilitation magnitude, respectively. The value of τ_2 ($\tau_2 \approx 27.902$) obtained from the fitting curve is about one magnitude larger than τ_1 ($\tau_1 \approx 1.449$), which is consistent with the PPF decaying process in a biosynapse.^[18] In addition, PPF behavior obtained under green light stimulation is shown in Figure S6 (Supporting Information). Compared with the results under UV illumination, a decrease of PPF index and fast decaying process with time intervals are observed, which suggests that the memory formation could be accelerated by the UV light stimulation.

There are two types of basic memory behavior in a biological neural system, which are short-term memory (STM) and long-term memory (LTM).^[19] The STM can only last from a few

milliseconds to a few seconds and then fade away completely, while the LTM usually persists for seconds or even years.^[20] Through applying repeated training and rehearsal, the STM could be transitioned to the LTM. This transition for the ZAC-OSs array was achieved by using pulsed UV light stimulation with various frequencies and pulse numbers, as shown in Figure 2c,d, respectively. With increasing the frequency or pulse number, the EPSC is gradually reinforced from weak (STM) to strong (LTM). Meanwhile, the decaying process of the EPSC is also confirmed to be slowed down with frequency and pulse number through the extracted relaxation time (Figure S7, Supporting Information), which proves the transition from STM to LTM. This transition could be also realized with different

frequencies or pulse numbers of the green light stimulation (Figure S8, Supporting Information). Figure 2e demonstrates the implementation of the “learning-experience” behavior of human brains on the ZAC-OSs array. We adopt two light pulse training processes with a certain time interval to simulate the device. The EPSC was gradually potentiated by the first training process (58 light pulses), representing the first learning process. And then, after EPSC decaying for 30.704 s, only 40% of EPSC change remained, implying that partial information has been forgotten. Next, in the second training process, 14 light pulses were utilized to recover the decayed EPSC, which is much fewer than the 58 pulses required in the first training process. However, after the second stimulation process, it needed a longer time to decay to the same EPSC value as the first forgetting process. This behavior is an analogy to the fact that relearning the forgotten information is much easier than the learning process the first time and the memory could be strengthened through repeating the learning process. The “learning-experience” behavior can also be implemented under green light stimulation (Figure S9, Supporting Information).

In biological neural networks, neuromodulators play a ubiquitous role in regulating synaptic plasticity to achieve high efficiency in information processing (Figure 3a).^[21] The piezo-phototronic effect, which can effectively tune the optoelectronic process of charge carriers through modulation of the energy band alignment at the junction,^[22] is utilized to implement the function of the neuromodulators. Upon applying external strain on the ZAC-OSs device, the piezoelectric polarization charges are induced at the two ends of ZnO NWs to tune the transport process of photogenerated charge carriers at the ZnO/Al₂O₃/CdS heterojunction, and consequently to regulate the synaptic plasticity, as shown in Figure 3b. The PPF index under different compressive pressure is depicted in Figure 3c. With increasing the external pressure, the PPF index at each time interval is reinforced, and the large pressure induces a slow decay trend of the PPF index with time intervals. This phenomenon can be explained by the photoresponse behavior with a single UV pulse (2.48 mW cm⁻², duration: 0.5 s) under different compressive pressures. As shown in Figure 3d, under strain-free conditions, the EPSC increases rapidly upon UV stimulation and an EPSC change of 0.55 μA is achieved, due to the generation of electron–hole pairs. After removing the UV stimulation, the EPSC decays gradually to its initial state within the 50s. Under the strained condition, both the initial current and the change of EPSC are decreased, while a long relaxation time of EPSC is obtained. Specifically, with the compressive pressure increasing from 0 to 24.5 MPa, the changes of EPSC reduce from 0.55 to 0.39 μA, confirming the modulation of the synaptic weight by the external pressure. However, the retained EPSC after decaying for 50 s increases with the compressive pressure. The extended relaxation time of the EPSC under the large pressure condition was confirmed through fitting the decayed EPSC with Kohlrausch stretched-exponential function (Figure S10, Supporting Information). This attributes to the upwards-bent band diagram at the heterojunction retards the recombination process of photoinduced electrons and holes. Thus, the EPSC evoked by the second light pulse increased with the external compressive strain, leading to the improvement of the PPF index (Figure 3c). Similar results were also observed under the

green light stimulation (Figure S11, Supporting Information). The “learning-experience” behavior was also characterized on the strained device under the compressive pressure of 24.5 MPa by using the same light stimulation condition with the strain-free devices (Figure 3e). In the first training process, the EPSC of the strained device was potentiated by 116 light pulses. After the first forgetting process for 37.775 s, it needed 18 light pulses to recover the decayed EPSC. Then, a longer decaying time of 44.515 s was observed at the second forgetting state. Compared with the behavior of the strain-free device in Figure 2e, the strained one needs more facilitation pulses to reach a similar EPSC level at the first training process, and a comparable number of light pulses are required during the relearning process. However, the relaxation time at the two forgetting processes was extended by 23.03% and 30.08%, respectively.

The working mechanism of the modulation of synaptic weight through the piezo-phototronic effect was thoroughly investigated by characterizing the *I*–*V* curves of the device and analyzing the tunneling effect at the ZnO/Al₂O₃/CdS heterojunction, as shown in Figure 4. Figure S12a (Supporting Information) illustrates the band diagram of the ZAC-OSs device, showing the type II band alignment between ZnO and CdS.^[15a,23] A depletion zone at the interface is formed due to the diffusion of charge carriers to realize a stabilized Fermi energy level under thermal equilibrium when the ZnO NWs are in contact with the CdS film. Three typical conduction mechanisms are considered here, which are the direct tunneling (DT) model, Fowler–Nordheim tunneling (FNT) model, and trap-assisted tunneling (TAT) model, as shown in Figure S12b (Supporting Information).^[24] When the forward bias voltage (*V*) is smaller than the tunneling barrier height (Φ_B), the barrier is deformed slightly and can maintain its original trapezoidal shape, and thereby the DT current is prominent at low voltage (Figure S12b(i), Supporting Information). With the *V* increasing to exceed Φ_B , the barrier is bent to be the triangle shape to further decrease the tunneling distance, and then the FNT occurs (Figure S12b(ii), Supporting Information). The dependence of the DT current (*I*_{DT}) and the FNT current (*I*_{FNT}) on the bias voltage can be expressed by the following equations^[25]

$$I_{DT} \propto V \cdot \exp \left[-\frac{4\pi d \sqrt{m^* \Phi_B}}{h} \right] \quad (3)$$

$$I_{FNT} \propto V^2 \cdot \exp \left[-\frac{8\pi d \sqrt{2m^* \Phi_B^3}}{3heV} \right] \quad (4)$$

where *m*^{*}, *h*, and *d* are the effective electron mass, Planck constant, and tunneling distance, respectively.

The *I*–*V* curves of the ZAC-OSs device can be reconfigured to the FN plot, defined as a plot of ln(*I*/*V*²) versus 1/*V*, to depict the transition from DT to FNT. By using the FN plot, Equation (4) can be rewritten in a linear relationship as

$$\ln \left(\frac{I_{FNT}}{V^2} \right) \propto -\frac{1}{V} \quad (5)$$

According to Equation (5), ln(*I*/*V*²) versus 1/*V* of the ZAC-OSs device under various strain conditions with UV illumination of 2.48 mW cm⁻² is plotted in Figure 4a. Under the strain-free condition, only the logarithmic growth is observed, which

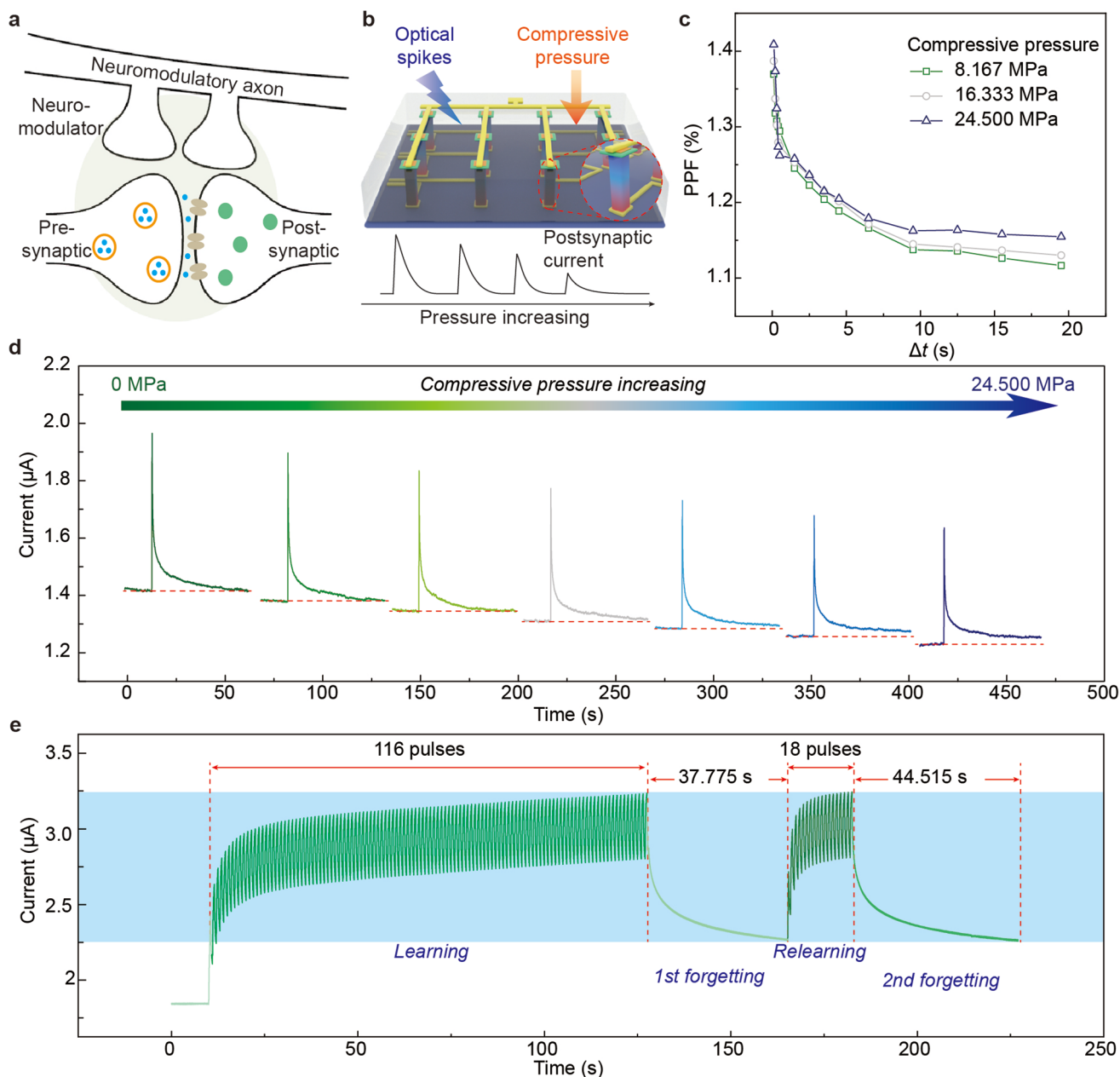


Figure 3. Modulation of the synaptic behavior of ZAC-OSs device under UV light stimuli by piezo-phototronic effect. a) Schematic illustration of the biological neuromodulator. b) Schematic illustration of the ZAC-OSs device under compressive pressure showing the modulation of the EPSC. c) PPF index as a function of the time interval of paired UV light under different compressive pressure conditions. d) The photoresponse behavior with a single UV light stimulation under various strain conditions. e) The modulated “learning-experience” behavior by piezo-phototronic effect under UV light stimuli.

suggests that the carrier transport process is dominated by DT. In contrast, the plot is divided by an inflection point into a linear decreasing regime and a logarithmic growth regime under the strained condition, indicating that the conduction mechanism has transited from DT to FNT with increasing bias voltage. However, under the high strain condition, a deviation from the linear decrease in the high voltage regime was observed, indicating the complex conduction mechanism of the device (Figure S13, Supporting Information). Considering the defects may be introduced inside the Al_2O_3 layer during

the device fabrication process, the trap-related model was also utilized to analyze the conductance origins. A generalized TAT model was adopted and the tunneling current (I_{TAT}) can be expressed as^[26]

$$I_{\text{TAT}} \propto \exp\left(\frac{-8\pi\sqrt{2em_{\text{ox}}^*}\Phi_1^{3/2}}{3hE}\right) \quad (6)$$

where m_{ox}^* is the effective electron mass in the Al_2O_3 layer and Φ_1 is the trap energy level. The TAT plot ($\ln I$ vs $1/E$) of the I - V

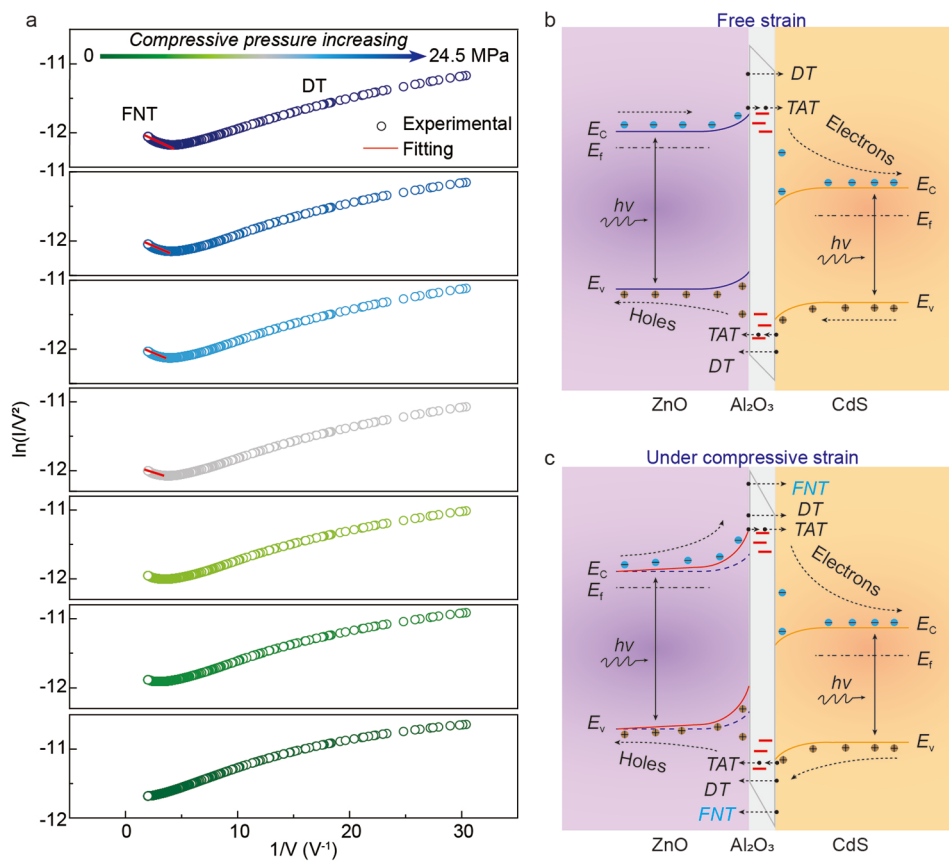


Figure 4. The working mechanism of the piezo-phototronic effect on the modulation of the synaptic behavior. a) Fowler–Nordheim plot of the ZAC-OSs device showing the transition from DT to FNT with increased compressive pressure. b,c) Band diagram of the ZnO/Al₂O₃/CdS heterojunction under strain-free and compressive strain conditions where the carriers tunneling mode was transformed from the DT and TAT mode to the coupling mode of DT, TAT, and FNT.

curves of the ZAC-OSs device is shown in Figure S14 (Supporting Information). In the high voltage regime, all the I – V curves can be well fitted using the TAT plot, confirming the validity of the TAT model and the slope of each curve maintained unchanged, indicating that the external strain did not change the TAT process. In the low voltage regime, the trapezoidal barrier tunneling current cannot be fitted with the TAT model in Equation (6). In addition, Schottky emission and Poole–Frenkel emission are also utilized to analyze the current origins, however, the extracted relative permittivity of Al₂O₃ is much larger than the values reported by other literatures, hence, these two models are not the conductive mechanism of the ZAC-OSs device. Thus, it is concluded that under high strain conditions, the current originated from the electrons tunneling through the FNT and TAT process, while the DT was the dominant mechanism under the strain-free condition.

To elaborate on the underlying physical process of piezo-phototronic induced transition of the transport mechanism, the band diagrams of the ZnO/Al₂O₃/CdS junction under strain-free and strained conditions are plotted in Figure 4b,c, respectively. As shown in Figure 4b, the electron–hole pairs could be generated in both ZnO NWs and CdS film under UV light stimulation. Under the forward bias voltage, the photoinduced electrons from the ZnO NWs and photoinduced holes

from CdS film will transport through the barrier by the DT and TAT effect and be collected by the electrodes, consistent with the logarithmic growth in the bottom panel of Figure 4a. Upon applying compressive pressure on the ZAC-OSs device, negative piezoelectric charges were introduced at the interface of ZnO/Al₂O₃, and positive piezoelectric charges were introduced at the bottom end of ZnO NWs. These piezoelectric charges would only be partially screened by the local free carriers.^[10c] Thus, the local negative piezoelectric charges bend the conduction and valence band of ZnO upwards and reduce the effective tunneling thickness, increasing the probability of the FNT effect (Figure 4c). On the other hand, the enhanced barrier height can generally reduce the possibility of photo-induced electrons from the ZnO NWs to transport through the junction and enhance the trapping of photoinduced holes from CdS film at the ZnO/Al₂O₃ interface.^[15b] Consequently, both the initial current and the change of EPSC are decreased while the relaxation time is extended with the increasing compressive pressure on the device.

With the regulation of the synaptic weight by the piezo-phototronic effect, the ZAC-OSs device can be utilized to implement the image recording, memorization, and recognition functions of the human visual-perception system. **Figure 5a** illustrates the circuit diagram of a customized multichannel

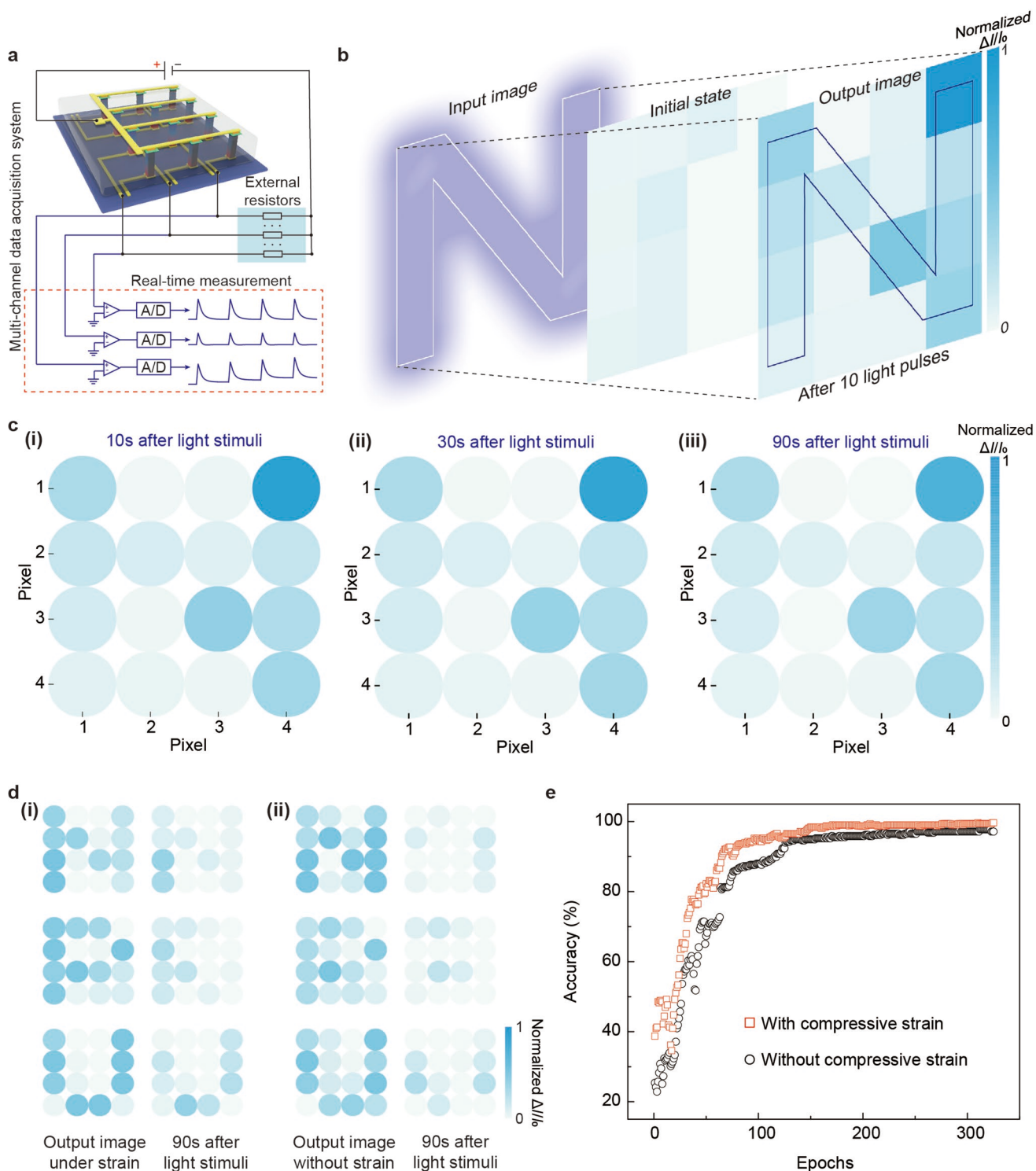


Figure 5. Piezo-phototronic effect modulated image visualization, recording, and recognition. a) Simplified electrical circuit of a customized multi-channel data acquisition system. b) EPSC of the ZAC-OSs array to show the distribution of 10 UV light pulses under the compressive pressure strain of 24.5 MPa. c) Information memorization behavior of the ZAC-OSs array after UV light stimuli. d) Examples of the training dataset include the output and decayed images recorded by the ZAC-OSs array under (i) and without (ii) compressive strain. e) Comparison of the recognition rate of the ZAC-OSs array with and without piezo-phototronic effect modulation.

data acquisition system, which can monitor the EPSC change of 16 pixels simultaneously. To introduce the piezo-phototronic effect, an “N”-shaped UV light stimulation with a pulse width

of 0.5 s, frequency of 1 Hz, and intensity of 2.48 mW cm^{-2} was applied on the device from the bottom glass substrate and external compressive pressure of 24.5 MPa was introduced on

the top surface of the device through a sapphire substrate, as shown in Figure S15 (Supporting Information). After applying 10 UV light pulses, the “N”-shaped input image could be easily recorded through mapping the change ratio contrast of the EPSC ($\Delta I/I_0$) (Figure 5b). Moreover, the recorded input image could be completely preserved. As shown in Figure 5c, the “N”-shaped image stored by the device for 90 s, could be easily recognized. In contrast, the device without piezo-phototronic effect modulation can only record the input image and store it for a short period. Figure S16 (Supporting Information) demonstrates the output image under strain-free condition, showing a more legible image of the input pattern after 10 light pulses but fading away within 60 s. These characteristics confirm the reliable imaging capability of the input pattern and the stable memorization effect of the ZAC-OSs device through the piezo-phototronic effect.

In the human visual system, the light information is first detected and pre-processed by the retina, and then transmitted to the visual cortex for image processing. To emulate this function, we combined a ZAC-OSs device and an artificial neural network. As shown in Figure S17 (Supporting Information), the input images were detected and memorized by the ZAC-OSs device, and then transported to the artificial neural network, which consists of an input layer (16), hidden layer (10), and output layer (3), for the image recognition task. To train and test the networks, we prepared six data sets with images of the letter “N”, “P”, and “U” acquired from the ZAC-OSs device with (Figure 5d (i)) and without compressive strain (Figure 5d (ii)). Each data set contains both the output images and the images stored for 90 s (350 images in total), which is randomly divided into the training data set (250 images) and the validation dataset (100 images). At every epoch, the 750 different training images were applied to the network, and the recognition rate was estimated by the 300 test images. Figure 5e demonstrates the recognition rate of the visual system under strain and strain-free conditions. Compared with the strain-free conditions, the train epochs for achieving 95% accuracy are reduced by 36.13% with the piezo-phototronic effect modulation. Furthermore, the rate with the piezo-phototronic effect can be eventually stabilized at 99.68% after 300 epochs while the maximum rate of 97.14% is obtained under the stain-free condition, illustrating the improvement of efficiency and recognition rate by the piezo-phototronic effect.

Furthermore, the device could extract the target image from the massive noisy optical inputs after preprocessing with the piezo-phototronic effect. As shown in Figure 6a, a set of noisy optical inputs (I_m) is applied on each pixel (P_n , $n = 1-16$) of the ZAC-OSs device, generating a differently weighted photocurrent (I_n , $n = 1-16$). Here, we adopt 16 noisy optical inputs to demonstrate its operating principle (Figure S18, Supporting Information). After applying 16 noisy optical inputs, the area consistent with the target image shape (pixels of #1, #4, #5, #6, #8, #9, #11, #12, #13, and #16) could receive 15 optical pulses, thus leading to a highly weighted photocurrent, whereas other pixels (pixel of #2, #3, #7, #10, #14, and #15) were only stimulated by one optical pulse and thereby generating a negligible photocurrent. Figure 6b presents the summary EPSC from each pixel, and the preprocessed images could be obtained by mapping the photocurrent at the final stage. The output images

generated by different noisy inputs are illustrated in Figure 6c, showing a gradually completed image pattern as well as the enhanced contrast with increasing the noisy optical inputs. Finally, the preprocessed “N”-shaped image is extracted from the noisy optical inputs, which is identical to its target image. The redundant data induced by the noisy input has been filtered and will not be transmitted to the subsequent processing stages, which ensures the high efficiency of the postprocessing. These characteristics of the ZAC-OSs device promise its potential application in robotic vision, neuromorphic computing, adaptive visual-perception systems, etc.

3. Conclusion

In summary, we demonstrated a two-terminal artificial OSs array based on the two-terminal ZnO/Al₂O₃/CdS heterojunction, which could be potentiated by both UV and green light stimulation in a wide intensity range. The synaptic weight of the device could be modulated by the external strain through the piezo-phototronic effect, resulting in a reinforced PPF index and prolonged photocurrent decay. The demonstrations of image acquisition proved that the input image could be recorded, memorized, and recognized with the piezo-phototronic effect and redundant noisy data could be filtered by the neuromorphic preprocessing of the device. This ZAC-OSs device provides a novel approach to regulate the synaptic behavior based on the simple two-terminal device with neuromorphic preprocessing, which renders it a promising building block for artificial adaptive visual-perception systems and neuromorphic computing.

4. Experimental Section

Fabrication of the ZAC-OSs Device: The fabrication process of the synapse device started with a standard cleaning process of the glass substrate. A glass substrate with the dimension of 35 mm × 25 mm × 1 mm was cleaned with acetone, isopropanol, and deionized water sequentially, and then was blown dry with nitrogen. Then, the bottom electrode array was defined by the conventional photolithography (Suss MA6 mask aligner), followed by the ITO film deposition through RF magnetron sputtering (Kurt J. Lesker, PVD75). A layer of ZnO seed film was defined with the dimension of 20 μm × 20 μm and a spacing of 300 μm and was aligned with the ITO electrodes array. The synthesis of the ZnO NWs array then occurred at 90 °C for 4 h in the solution containing 20 × 10⁻³ M zinc nitride (Sigma-Aldrich) and 20 × 10⁻³ M hexamethylenetetramine (HMTA) (Alfa Aesar). After the NWs growth, a SU-8 thin film was spin-coated on the as-fabricated device and followed by a hardbake process at 135 °C for 2 h to improve mechanical robustness. Next, the SU-8 residue was etched by oxygen plasma treatment to expose the top end of NWs and an 8-nm-thick Al₂O₃ film was deposited on the NWs array through an atomic layer deposition (ALD) system. Then, a CdS film array and an ITO top electrode array were formed and well-aligned with ZnO NWs through repeating the photolithography and sputtering deposition process. A thin encapsulation layer of polyvinyl butyral (PVB) was spin-coated on the active area to complete the device fabrication.

Experimental Setup and Materials Characterization: A customized measurement system, which contained two nanopositioning stages (Newport, M462), a probe station (Semiprobe, M6), a hard metal pole, an electric dynamometer, and a light source based on two LEDs with the emission wavelength of 365 and 525 nm, respectively, was designed. The external pressure was applied through controlling the nanopositioning

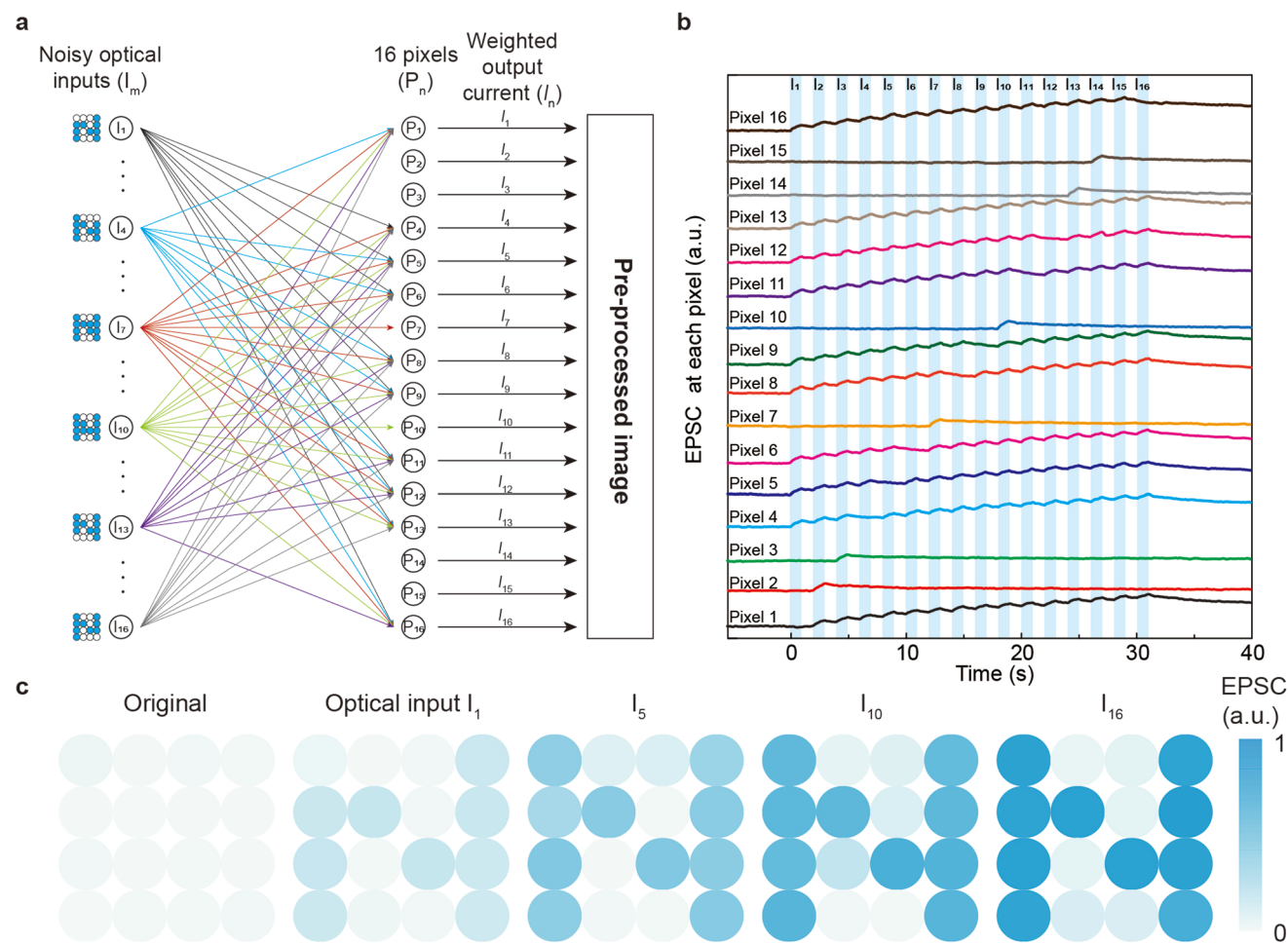


Figure 6. Neuromorphic image preprocessing during the acquisition process. a) Schematic illustration of the image acquisition and preprocessing of the ZAC-OSs device with 16 noisy optical inputs. b) Normalized EPSC of each pixel of the ZAC-OSs device. c) Output images after each optical input. I_{16} represents the preprocessed image by the ZAC-OSs device.

stage to tune the position of the hard metal pole and press a sapphire substrate on the top surface of the device and the pressure was recorded by the dynamometer simultaneously. The light pulses were controlled by a waveform generator (National Instrument, PXIe 5433) and were applied to the bottom surface of the device through the designed photomask. The electrical characterization of a pixel was performed through a function generator (Stanford, DS345) and a current amplifier (Stanford, SR570). All the pixels of the device were individually addressable and the light pulse distribution was obtained through the multichannel testing system (National Instrument, PXIe 4300). The morphology images of the ZnO NWs array were recorded using the scanning electron microscope (Hitachi, SU8020). The absorbance spectra of different layers of the device were measured using the UV-vis-NIR spectrometer (Shimadzu UV-3600).

Supporting Information

Supporting Information is available from the Wiley Online Library or from the author.

Acknowledgements

The authors thank the support of Guangdong Basic and Applied Basic Research Foundation (2020A1515110740), National Natural Science Foundation of China (Nos. 52125205, U20A20166, 52192614, and

52102184), National key R&D program of China (2021YFB3200302 and 2021YFB3200304), Natural Science Foundation of Beijing Municipality (Z180011 and 2222088), Shenzhen Science and Technology Program (Grant No. KQTD20170810105439418), and the Fundamental Research Funds for the Central Universities.

Conflict of Interest

The authors declare no conflict of interest.

Data Availability Statement

The data that support the findings of this study are available from the corresponding author upon reasonable request.

Keywords

image preprocessing, neuromodulator, optoelectronic synapses arrays, tunable synaptic weight, two-terminal

Received: September 20, 2022

Revised: November 29, 2022

Published online:

- [1] a) H. Markram, *Nat. Rev. Neurosci.* **2006**, *7*, 153; b) M. M. Waldrop, *Nature* **2016**, *530*, 144.
- [2] a) P. A. Merolla, J. V. Arthur, R. Alvarez-Icaza, A. S. Cassidy, J. Sawada, F. Akopyan, B. L. Jackson, N. Imam, C. Guo, Y. Nakamura, B. Brezzo, I. Vo, S. K. Esser, R. Appuswamy, B. Taba, A. Amir, M. D. Flickner, W. P. Risk, R. Manohar, D. S. Modha, *Science* **2014**, *345*, 668; b) X. Liao, L. Xiao, C. Yang, Y. Lu, *Front. Comput. Sci.* **2014**, *8*, 345.
- [3] a) T. Hasegawa, T. Ohno, K. Terabe, T. Tsuruoka, T. Nakayama, J. K. Gimzewski, M. Aono, *Adv. Mater.* **2010**, *22*, 1831; b) C.-S. Poon, K. Zhou, *Front. Neurosci.* **2011**, *5*, 108; c) H. Han, H. Yu, H. Wei, J. Gong, W. J. S. Xu, *Small* **2019**, *15*, 1900695.
- [4] a) S. Dai, Y. Zhao, Y. Wang, J. Zhang, L. Fang, S. Jin, Y. Shao, J. Huang, *Adv. Funct. Mater.* **2019**, *29*, 1903700; b) H. Yu, H. Wei, J. Gong, H. Han, M. Ma, Y. Wang, W. Xu, *Small* **2021**, *17*, 2000041; c) X. Han, Z. Xu, W. Wu, X. Liu, P. Yan, C. Pan, *Small Struct.* **2020**, *1*, 2000029.
- [5] a) A. E. Pereda, *Nat. Rev. Neurosci.* **2014**, *15*, 250; b) D. A. McCormick, D. B. Nestvogel, B. J. He, *Annu. Rev. Neurosci.* **2020**, *43*, 391.
- [6] a) M. Lee, W. Lee, S. Choi, J.-W. Jo, J. Kim, S. K. Park, Y.-H. Kim, *Adv. Mater.* **2017**, *29*, 1700951; b) Y. Wang, Z. Lv, J. Chen, Z. Wang, Y. Zhou, L. Zhou, X. Chen, S.-T. Han, *Adv. Mater.* **2018**, *30*, 1802883; c) X. Han, W. Wu, H. Chen, D. Peng, L. Qiu, P. Yan, C. Pan, *Adv. Funct. Mater.* **2021**, *31*, 2005230.
- [7] a) S. Qin, F. Wang, Y. Liu, Q. Wan, X. Wang, Y. Xu, Y. Shi, X. Wang, R. Zhang, *2D Mater.* **2017**, *4*, 035022; b) R. A. John, F. Liu, N. A. Chien, M. R. Kulkarni, C. Zhu, Q. Fu, A. Basu, Z. Liu, N. Mathews, *Adv. Mater.* **2018**, *30*, 1800220; c) Z.-D. Luo, X. Xia, M.-M. Yang, N. R. Wilson, A. Gruverman, M. Alexe, *ACS Nano* **2020**, *14*, 746.
- [8] a) X. Li, M. Chen, R. Yu, T. Zhang, D. Song, R. Liang, Q. Zhang, S. Cheng, L. Dong, A. Pan, *Adv. Mater.* **2015**, *27*, 4447; b) Z. Wang, R. Yu, C. Pan, Y. Liu, Y. Ding, Z. L. Wang, *Adv. Mater.* **2015**, *27*, 1553; c) Z. Yang, M. Jiang, L. Guo, G. Hu, Y. Gu, J. Xi, Z. Huo, F. Li, S. Wang, C. Pan, *Nano Energy* **2021**, *85*, 105951; d) R. Zhou, G. Hu, R. Yu, C. Pan, Z. L. Wang, *Nano Energy* **2015**, *12*, 588.
- [9] a) X. Han, W. Du, R. Yu, C. Pan, Z. L. Wang, *Adv. Mater.* **2015**, *27*, 7963; b) X. Han, M. Chen, C. Pan, Z. L. Wang, *J. Mater. Chem. C* **2016**, *4*, 11341; c) Q. Zhang, S. Zuo, P. Chen, C. Pan, *InfoMat* **2021**, *3*, 987; d) J. Sun, Q. Hua, R. Zhou, D. Li, W. Guo, X. Li, G. Hu, C. Shan, Q. Meng, L. Dong, *ACS Nano* **2019**, *13*, 4507.
- [10] a) C. Pan, M. Chen, R. Yu, Q. Yang, Y. Hu, Y. Zhang, Z. L. Wang, *Adv. Mater.* **2016**, *28*, 1535; b) X. Han, W. Du, M. Chen, X. Wang, X. Zhang, X. Li, J. Li, Z. Peng, C. Pan, Z. L. Wang, *Adv. Mater.* **2017**, *29*, 1701253; c) C. Pan, J. Zhai, Z. L. Wang, *Chem. Rev.* **2019**, *119*, 9303; d) R. Bao, J. Tao, C. Pan, Z. L. Wang, *Small Sci.* **2021**, *1*, 2000060; e) C. Pan, L. Dong, G. Zhu, S. Niu, R. Yu, Q. Yang, Y. Liu, Z. L. Wang, *Nat. Photonics* **2013**, *7*, 752.
- [11] G. Wang, R. Wang, W. Kong, J. Zhang, *Cogn. Neurodyn.* **2018**, *12*, 615.
- [12] a) V. M. Ho, J.-A. Lee, K. C. Martin, *Science* **2011**, *334*, 623; b) L. F. Abbott, W. G. Regehr, *Nature* **2004**, *431*, 796.
- [13] a) J. Bao, I. Shalish, Z. Su, R. Gurwitz, F. Capasso, X. Wang, Z. Ren, *Nanoscale Res. Lett.* **2011**, *6*, 404; b) D. Azulay, O. Millo, S. Silbert, I. Balberg, N. Naghavi, *Appl. Phys. Lett.* **2005**, *86*, 212102.
- [14] J. C. Phillips, *Rep. Prog. Phys.* **1996**, *59*, 1133.
- [15] a) F. Zhang, Y. Ding, Y. Zhang, X. Zhang, Z. L. Wang, *ACS Nano* **2012**, *6*, 9229; b) F. Zhang, S. Niu, W. Guo, G. Zhu, Y. Liu, X. Zhang, Z. L. Wang, *ACS Nano* **2013**, *7*, 4537; c) S. Qiao, J. Liu, G. Fu, K. Ren, Z. Li, S. Wang, C. Pan, *Nano Energy* **2018**, *49*, 508.
- [16] L. Q. Zhu, C. J. Wan, L. Q. Guo, Y. Shi, Q. Wan, *Nat. Commun.* **2014**, *5*, 3158.
- [17] H. K. Li, T. Chen, P. Liu, S. Hu, Y. Liu, Q. Zhang, P. S. J. Lee, *J. Appl. Phys.* **2016**, *119*, 244505.
- [18] R. S. Zucker, W. G. Regehr, *Annu. Rev. Physiol.* **2002**, *64*, 355.
- [19] a) S. Gao, G. Liu, H. Yang, C. Hu, Q. Chen, G. Gong, W. Xue, X. Yi, J. Shang, R.-W. Li, *ACS Nano* **2019**, *13*, 2634; b) L. Zhao, Z. Fan, S. Cheng, L. Hong, Y. Li, G. Tian, D. Chen, Z. Hou, M. Qin, M. Zeng, X. Lu, G. Zhou, X. Gao, J.-M. Liu, *Adv. Electron. Mater.* **2020**, *6*, 1900858.
- [20] S. Li, F. Zeng, C. Chen, H. Liu, G. Tang, S. Gao, C. Song, Y. Lin, F. Pan, D. J. Guo, *J. Mater. Chem. C* **2013**, *1*, 5292.
- [21] V. Pedrosa, C. Clopath, *Front. Synaptic Neurosci.* **2017**, *8*, 38.
- [22] R. Bao, J. Tao, C. Pan, Z. L. Wang, *Small Sci.* **2021**, *1*, 2000060.
- [23] F. Xu, V. Volkov, Y. Zhu, H. Bai, A. Rea, N. V. Valappil, W. Su, X. Gao, I. L. Kuskovsky, H. Matsui, *J. Phys. Chem. C* **2009**, *113*, 19419.
- [24] a) H.-M. Li, D. Lee, D. Qu, X. Liu, J. Ryu, A. Seabaugh, W. J. Yoo, *Nat. Commun.* **2015**, *6*, 6564; b) G. Nazir, H. Kim, J. Kim, K. S. Kim, D. H. Shin, M. F. Khan, D. S. Lee, J. Y. Hwang, C. Hwang, J. Suh, J. Eom, S. Jung, *Nat. Commun.* **2018**, *9*, 5371; c) H. Spahr, S. Montzka, J. Reinker, F. Hirschberg, W. Kowalsky, H.-H. Johannes, *J. Appl. Phys.* **2013**, *114*, 183714.
- [25] T. Ikuno, H. Okamoto, Y. Sugiyama, H. Nakano, F. Yamada, I. J. A. P. L. Kamiya, *Appl. Phys. Lett.* **2011**, *99*, 023107.
- [26] M. P. Houn, Y. H. Wang, W. J. Chang, *J. Appl. Phys.* **1999**, *86*, 1488.